# Simulating HV-SEM imaging of HAR and buried features

Benjamin D. Bunday[a], Shari Klotzkin[b], Douglas Patriarche[c], Yvette Ball[a], Maseeh Mukhtar[d], Kotaro Maruyama[e], Seul-Ki Kang[e], Yuichiro Yamazaki[e]

[a]AMAG nanometro, Schenectady, NY, 12303, USA
[b]AMAG nanometro, Binghamton, NY, 13850, USA
[c]AMAG nanometro, Ottawa, ON, K2G 5M9, Canada
[d]KLA, Milpitas, CA, 95035, USA
[e]TASMIT/TORAY Inc., Yokohama-shi, Kanagawa-ken, Japan 222-0033

## ABSTRACT

In this work, important use cases for HV-SEM will be explored by simulation, such as HAR hole / trench imaging with various profiles and depths, buried feature imaging to understand detection and effective resolution with depth for optical overlay cases, and buried defect and void detection, using a new improved electron beam simulator which greatly extends utility of JMONSEL, AMAG SimuSEM, enabling many complex simulation scenarios to be achievable with many improved outputs and other augmentations. The use of simulation designed experiments (DOEs) to predict best conditions and performance for the above applications will be demonstrated, along with some physical validation in the HV-SEM process space for the JMONSEL/SimuSEM physics kernel by reproducing a few cases in the literature and to experimental results on recent AMAG7 HAR measurement targets.

**Keywords:** CD-SEM, HV-SEM, DI-SEM, JMONSEL, SimuSEM, HAR, contact, buried features, Monte Carlo simulation

## INTRODUCTION

After many years of industry reluctance to HV-SEM becoming a mainstream inline fab tool, HV-SEM has recently proven itself an important part of the inline metrology technique ecosystem for meeting many upcoming technical challenges, and is thus now becoming a common inline instrument with a growing list of valuable and crucial roles in current and future semiconductor fabrication with sensitivity to important CD, overlay and defect aspects. The ability to have an adequate resolution microscopy capable of detecting buried structures and locations, or of imaging down deep holes and trenches are very welcome, necessary and timely developments for various critical applications in VNAND manufacturing, where deep holes and trenches are the basic building blocks of measured features and which are known challenging metrology targets. Additionally, using HV-SEM see-thru imaging for calibrating optical overlay has become another key driving application for HV-SEM. Buried defect or void detection are additional cases where HV-SEM has value.

However, as HV-SEM is a relatively new arrival to inline quantitative metrology, it must be noted that the process space of tool parameters for different uses is an area that we as an industry will need to quickly learn to get the most value out of these new tools—every stack is likely a new measurement problem to solve. Experimentation can be done on a sample of interest to find best parameters, but doing a full physical/experimental DOE of a full process space (such as HAR holes of different depths) with a relatively broad range of different tool conditions (such as beam energy) is a costly and time-consuming exercise; Monte Carlo-based SEM simulations can be of much value for exploring such parameter spaces, as “the answer” of where features and edges are located is inherently known from the defined design, so the effects of the critical parameters in relating to those inputs can be directly understood.

In this work, a few of the most important use cases for HV-SEM will be explored, such as HAR hole and trench imaging with various profiles and depths, buried feature imaging to understand detection and effective resolution with depth for a few common materials sets of interest in the optical overlay cases, and buried defect and void detection will be explored using the SEM simulation software based on NIST’s JMONSEL [1-11], AMAG SimuSEM [12], which makes possible,

through its elegant and powerful GUI, detailed and thorough SEM simulation experiments with much utility, productivity, flexibility, visualization, accessibility, and achievable complexity of designed features with fast simulation speeds, including running on remote cloud resources at large scale. The use of simulation DOEs to predict best conditions and performance for the above applications will be demonstrated, along with some validation in the HV-SEM process space for the JMONSEL/SimuSEM physics kernel by reproducing a few cases in the literature by simulation, and to images of various recent AMAG7 HAR measurement targets [13].

## IMPORTANCE OF SEM SIMULATIONS

To fabricate in the nanoscopic size regime, one must be able to competently image and measure what is being built. Thus, the importance of improved metrology continues to grow as Moore's Law progresses and devices continue to shrink, become more complex with multiple layers and new include materials. Scanning Electron Microscopes (SEMs) image physical samples using scanning electron beams—electrons raster across solid objects and collect intensity/energy versus position information to form maps showing surface structure with possibly some depth information measuring backscattered electron yields.

SEM measurements are crucial in R&D and manufacturing of semiconductor chips. However, these types of measurements are very expensive, and simulation support helps chip manufacturers achieve measurements that improve manufacturing yield, are statistically significant enough to make process decisions, and save time and money accelerating development of next generation chips. SEM simulation capability will contribute to the metrology understanding necessary during IC device fabrication, both during development of new devices and manufacturing process control. The tightness of the distribution of widths of billions of transistors on a chip is only producible to tolerance with the appropriate process monitoring.

SEM metrology is the main workhorse technique for a fab's process control, and a fab's eyes to yield-killing defectivity. These tools are operating near resolution and speed limits, such that simulation support for understanding the measurements and images is critical to successful, constructive and stable metrology. SEM imaging and electron beam condition optimization is important for achieving the best signal to noise possible of the aspect of the feature under evaluation, and this optimum is very sample-type and condition dependent. Additionally, if exploring items not easy to build at time of interest, as is the case when process development begins, simulation is an inexpensive alternative to tailor-building tools to explore a trial condition, or have built to perfection applicable samples for physical imaging case studies, samples which might be items possible years in future which cannot be built very well at the time a preliminary study is needed. Simulation allows conclusive results for such studies due to the full knowledge of the user-defined sample, and at a very small fraction of the cost or time involved for physical experiments. Once validated, a SEM simulation model can be used to extrapolate similar imaging to mass produce images over an entire process window, which can be effective for dealing with models involving larger parameter spaces. Simulation thus allows predictions to target other efforts, along with other advantages such as tailored model-based algorithms to measure a given case of interest, which will be necessary to maintain accurate and precise measurements of features of sizes close to resolution limits at 5 nm and 3 nm nodes and beyond. Also, such simulations can be used to produce images for other purposes such as calibrating AI image analysis tools with faux images, studying the evolution of 2D shape contours of different features at different conditions, or for providing a standard for comparison to other metrologies thru physical data or comparison of simulation results. Also, SEM simulations are used to determine best SEM conditions for measurement or imaging of various applications, or understand issues in measuring various feature types. Recently, the advent of HV-SEM becoming mainstream fab tools has enabled ability to calibrate optical overlay with see-through SEM imaging, and simulators are valuable for understanding needed beam conditions to detect desired buried signals for different applications. SEM simulation is crucial for understanding the SEM metrology best practices, conditions and error sources which influence the success of metrology in such efforts.

## NIST JMONSEL & AMAG SimuSEM

Such SEM simulators have been available for awhile. JMONSEL, Java MONte Carlo Simulator for Secondary Electrons, is a 3D electron beam simulation software package developed and programmed in the 2010-12 timeframe at National Institute of Standards & Technology (NIST) by Dr. John Villarrubia using Java/JYTHON, funded by

SEMATECH AMAG to enable limits simulation studies for defect and critical dimension SEM metrology. NIST has supported ongoing improvement and validation efforts since, and it is now well validated for non-charging cases, with some use by a small user community.[1-12,14-19]

JMONSEL uses finite element analysis (FEA) to track primary electrons as they enter a material, scatter, lose energy, and generate secondary & backscattered electrons. By monitoring the electrons that exit the material and are captured by a detector (software counter element), the electron yields can be found at any point designated as a target pixel. The physical models in JMONSEL are the best-known models in the literature in the energy ranges used here, open-source, with complete transparency in their documentation, definition, implementation and execution, as programmed by NIST, with a decade of validation data and wide acceptance by the industry.

However, the primitive JMONSEL code does have shortcomings. The largest of these is lack of user-friendliness; gaining proficiency with the primitive JMONSEL code takes much time with a steep and long learning curve, and the sample definition functions, while simple at a basic level, can become extremely complex to visualize for the programmer when trying to design features of the complexity of modern-day device structures or any 3D shapes beyond a few basic included shape primitives, impractical to code on a large scale for complex features. It had only minimal visualization thru VRML viewed in a web browser, no graphical interface. Original JMONSEL required very rigorous, involved, detailed line-edited Jython scripts, that typically would be 600-1000 lines long or more, and were themselves full Jython programs that called up core JMONSEL functions. See Figure 1 of a small part of a Jython script to just define part of the substrate.

```
# Layer.s3
    location = [  0.000*meterspernm,  0.000*meterspernm,557.500*meterspernm]
    rotation = [  0.000*math.pi,  0.000*math.pi,  0.000*math.pi]
    dimensions = [500.000*meterspernm,500.000*meterspernm, 15.000*meterspernm]
    thickness3=location[2]+dimensions[2]/2
    layers3=mon.NormalMultiPlaneShape()
    layers3.addPlane(normalVector,[0,0,thickness2])
    layers3.rotate(location,-math.pi/2,rotation[0],math.pi/2)
    layers3.rotate(location,0,rotation[1],rotation[2])
    layers3region = monte.addSubRegion(layers2region,SiMSMDeep,layers3)
```

Figure 1: example few lines for describing a feature in a conventional pre-SimuSEM JMONSEL script which can be as long as 1000 lines of rigorous math and spatial relationships, with no means for visualization of the target other than trial and error which is very cumbersome and time-consuming, and with the extreme detail involved complex features are very challenging to define, if not practically impossible.

Another shortcoming of original JMONSEL was that it was not speed optimized; small images would take hours, and large projects could take days or months, especially when charging was attempted which ran so slow were deemed impractical. Old JMONSEL had issues with sometimes pixel times increasing with number of pixels such that larger jobs would gradually bog down and take very long to finish near the end.

To fully modernize JMONSEL and make it practical and very useful in current times, AMAG nanometro has introduced a software package called SimuSEM, which uses JMONSEL as its core physics but addresses JMONSEL's shortcomings by greatly improving the simulation run speed and providing a user-friendly front-end GUI and tools to visualize and analyze the results. SimuSEM, which includes many original improvements to JMONSEL, is a modern intuitive 3D graphical GUI which makes the code much more usable, with JMONSEL's runtime speed issues also addressed. This program provides the user with greatly improved utility, productivity, flexibility, visualization, accessibility, and achievable complexity of designed features while improving simulation speed and scalability, plus many other refinements and additions, and superior results access. Additionally, the new code allows viewing of all electron trajectories in the 3D environment and other nanoscopic views of the results. Thus, additional observations on how various process subtleties might affect the SEM signal can be studied. See Figure 2 for comparison to Figure 1 to see how all JMONSEL functionality is now built into Blender.[20] The improvement in simplification for the user, utility and visualization is obvious. All features are now reduced to best practices based on much experience using the code by the authors, who have built the SimuSEM GUI with accessibility to features and sample and results visualization as priorities.

Speed optimization of JMONSEL also got a major overhaul as a major targeted improvement, so in this project these issues have been addressed and the runtime simulation speed optimized >35x for a single core but with multithreading added, >5000x faster than original JMONSEL with confirmed unchanged outputs, and with the pixel time slowdown issue eliminated.

AMAG SimuSEM's GUI is realized by building all the core JMONSEL code for writing runnable JMONSEL simulation scripts directly into a contemporary widely-acclaimed open-source 3D modelling and graphics engine, Blender, along with GMSH mesh generation program. Blender is a flexible platform with very powerful game-quality graphics engine that is used in the entertainment industry such as for Cartoon Network animations and to design 3D shapes for 3D printing, but is also actually a very effective 3D Cartesian space object workbench which has recently been discovered by the scientific community as a way to create excellent geometries needed for 3D simulations. Blender is a great fit with JMONSEL as it supports Python addons, allowing JMONSEL to be directly incorporated and the interface customized to the application.[12,20] A Python program is being developed to customize JMONSEL into Blender's GUI to create a bridge between Blender and JMONSEL. The result is a 3D sample designing environment with definable virtual SEM functionality. Additional Python modules are installed to provide other functionality, including analysis and plots of simulation results viewable alongside Blender's 3D model. GMSH has a Python API to allow grid generation to be accessed through the customized GUI. By combining these programs, functionality that is already available does not need to be recreated and is standardized for common use.

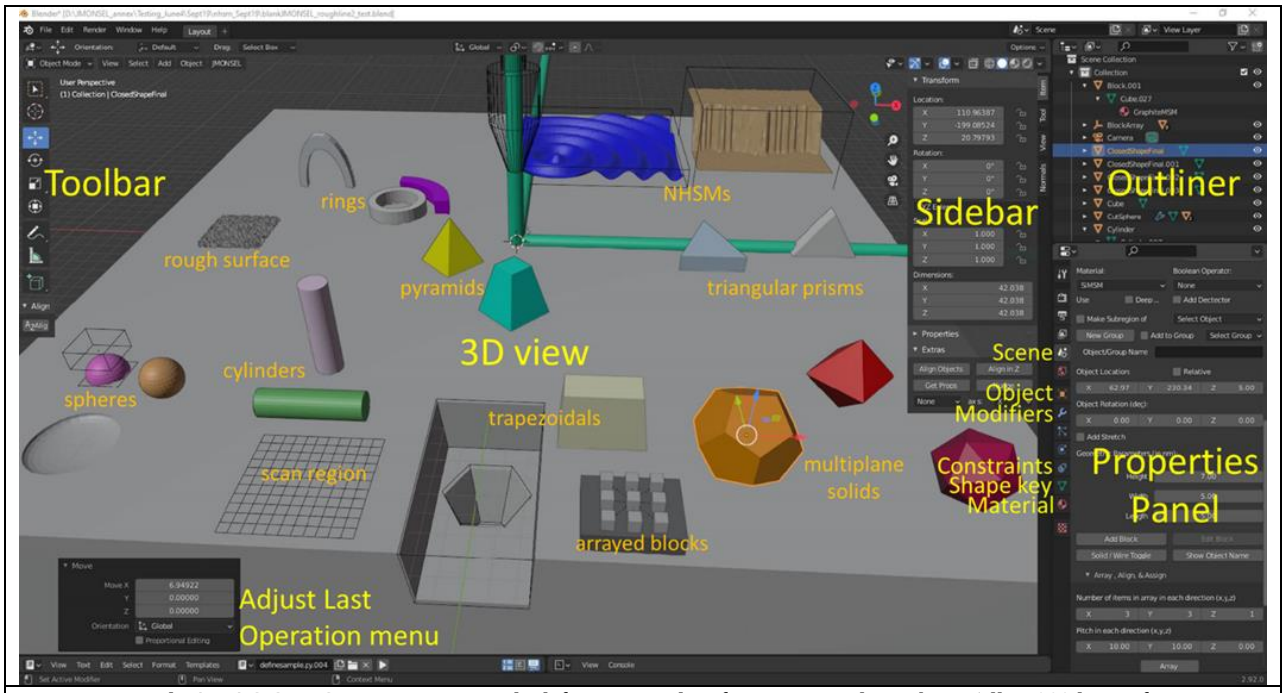


Figure 2: Example AMAG SimuSEM intuitive sample definition window for same sample as above (all ~1000 lines of script automatically produced for this shown sample by this constructor), which allows full 3D visualization at any scale or angle including see-thru mode, a good set of ready-to-use shape types, simple mouse-driven modification and many best JMONSEL practices and features plus new features with SimuSEM, with all routines built into a systematic package making all capabilities commonly available and ready for user deployment.

Another past shortcoming of JMONSEL which SimuSEM addresses with much improvement is the materials library—SimuSEM includes many new defined materials and the ability to add more with basic material information and with a few points of SE yield data, and also is expandable in future as NIST is bringing up a new material electron yield characterization laboratory which will output everything needed to produce new materials definitions from experimental samples.[21]

JMONSEL does have a charging model which is theoretically quite sound, but the past JMONSEL speed issues mean it has not been tested much and remains mostly unused in typical work. With the new speed improvements, charging will become a usable feature in SimuSEM. Another shortcoming was the moderate materials library, and the project also has plans in the works to improve that situation.

SimuSEM includes a large evolving list of shape primitives, all of which can be translated, rotated, scaled and defined parametrically but also with manual GUI manipulation by mouse. The user uses these and other constructions within the

GUI to easily construct sophisticated target designs and control the scanning regions with full control of beam parameters and pixel locations. Pixel locations are all directly viewable, and great care has been taken to confirm what shows in the Blender GUI window is exactly what is achieved in JMONSEL.

Addressing the lack of 3D visualization of the user's design with a modern GUI is important for the user to achieve applicable designs with complexity and detail. SimuSEM adds this all-important 3D visualization to JMONSEL. As a result, the complexity of the samples that can be created for a JMONSEL simulation without the GUI is extremely limited, and the time taken for a user to develop a complex or even simple design is much longer due to this lack of visualization. The core JMONSEL code has been validated over the last ten years and works well for the electron material interactions, however JMONSEL has sorely lacked a GUI front end that makes such a simulator much more usable and powerful. Adding the intuitive GUI and other improvements to JMONSEL, AMAG SimuSEM is the greatly accelerated, user-friendly, mature version of JMONSEL with rich and reliable visualization, with the scripting handled automatically, allowing even users with minimal SEM experience to transparently unlock this powerful code through the greatly improved interface. With the script rigor removed, JMONSEL, thru AMAG SimuSEM, is now modernized to address many more simulation cases with much more complexity as required for contemporary needs. Figure 4 shows some more example images of achievable complex features.

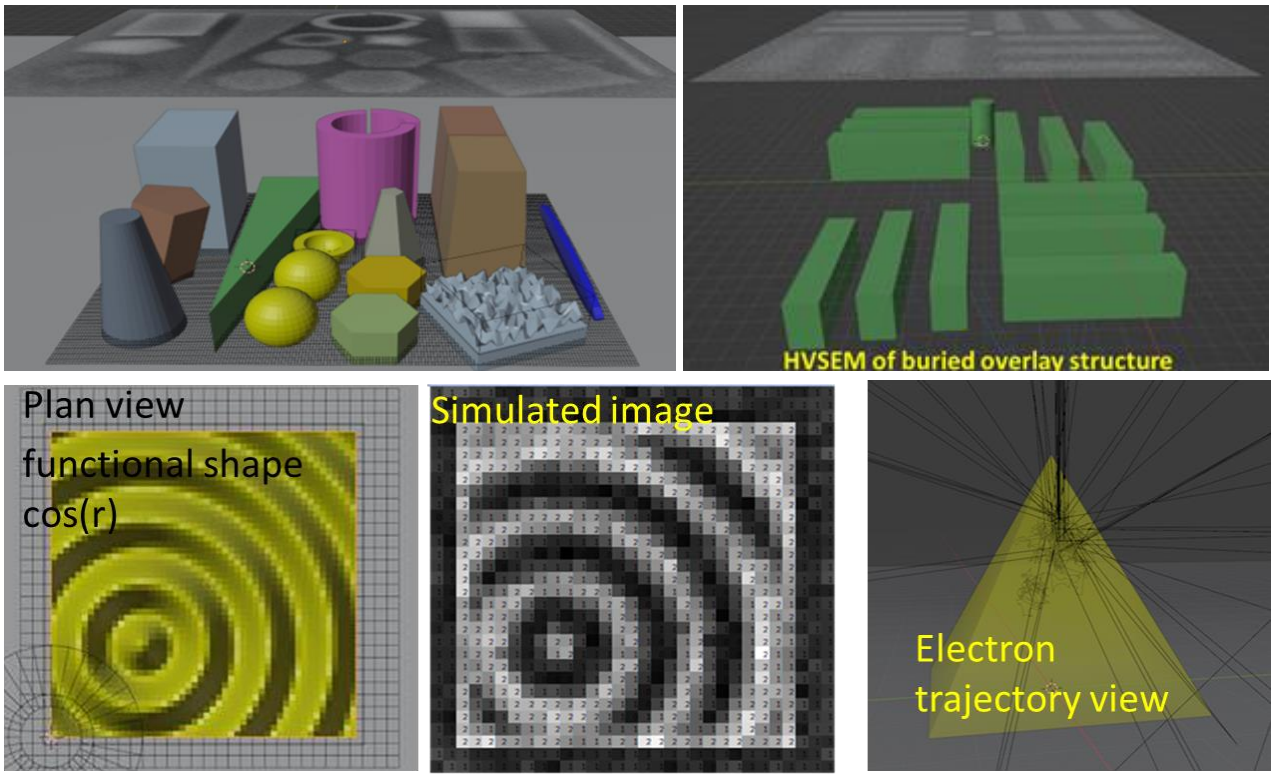


Figure 3: Image gallery showing achievable complexity of features in SimuSEM.

## VIRTUAL EXPERIMENTS

The goal of this simulation study is to demonstrate the capability to accurately simulate HV-SEM imaging for important use cases, by first validating SimuSEM in that regime against experimental HAR hole images from both experiment and in comparison to another study in the literature [22], and evaluate the signal to noise ratios (SNRs, sometimes also called contrast to noise ratio, or CNR) over DOEs of buried metal line gratings as with see-thru overlay and for detecting defects in a very complex sample for simulation, an ONO intentional defect array (IDA) for detectability in terms of SNR. SimuSEM allows the complexity to explore these cases that were impractical before.

## HAR HOLE EXPERIMENTAL & SIMUATION VALIDATION

First, we experimentally validate SimuSEM in the HV-SEM regime against experimental HAR hole images from both experiment and in comparison to another study in the literature [22].

AMAG nanometro also has its own product line of test wafers [13], and here we make use of AMAG7 HAR holes of 1 μm and 1.5 μm depths as validation targets for this study. The holes are patterned using the AMAG7 reticle and etched with features of interest being C60P120 (contact holes of nominal 60 nm diameter and 120 nm pitch), and slightly larger holes up thru C70P140. These targets were imaged for SE and BSE images by TORAY's NGR5000 HV-SEM at 10 keV incident beam. These experimental images are taken in grayscale, but viewing them with color scales that accentuate details at hole bottom shows rich quantitative signal content at the hole bottom, allowing estimation of bottom CD and hole tilt angle, as shown in the results in Figure 4.

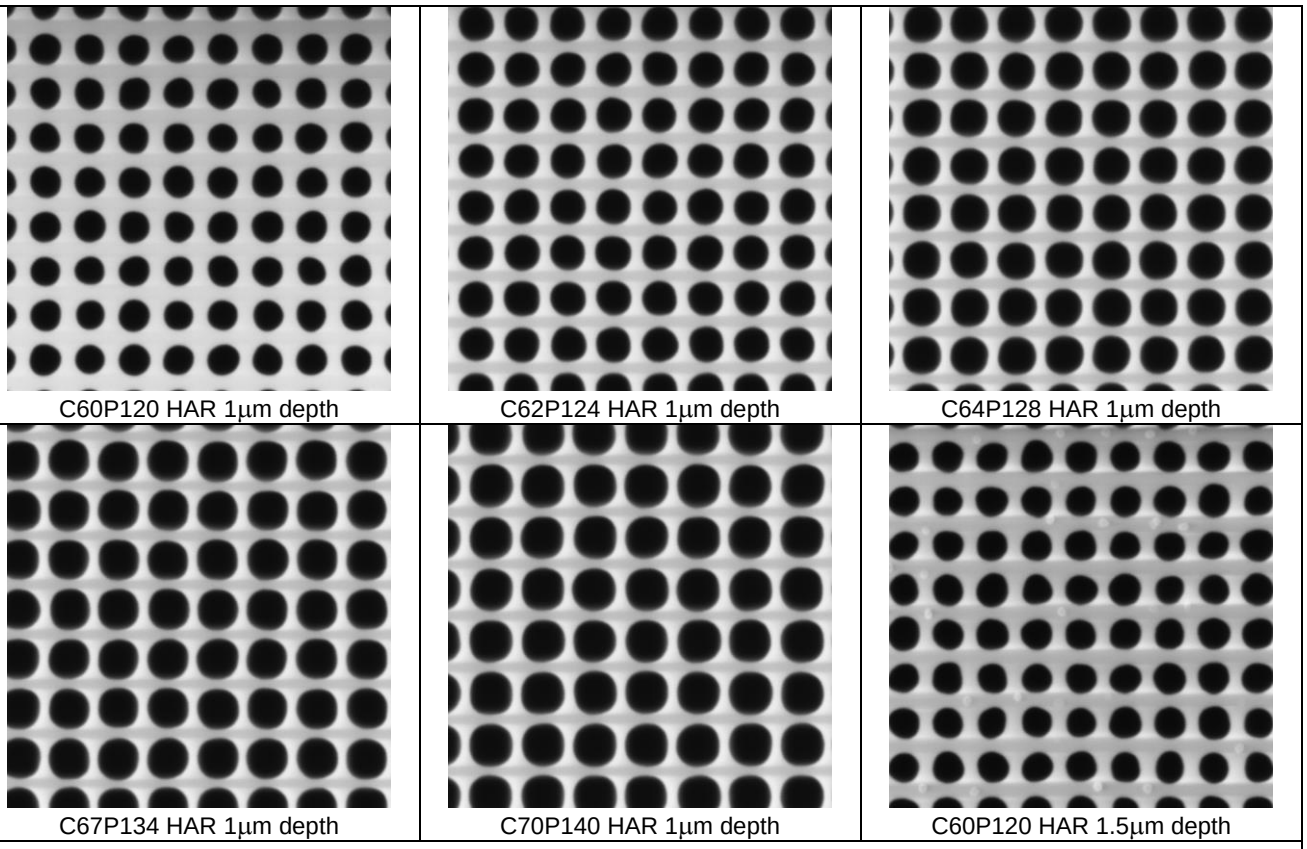


Figure 4: NGR5000 topdown HV-SEM images of AMAG7 HAR hole samples [13] of 1μm and 1.5μm depths, with lateral dimensions as marked.

To validate SimuSEM, images at the same conditions were be simulated and the resulting waveforms compared to those taken from the above images. To simulate the correct profiles, the XSEM image of the features is loaded into SimuSEM and properly-scaled, and compound 2-cone models for the holes are defined directly over the profile as a first estimate of dimensions to simulate.

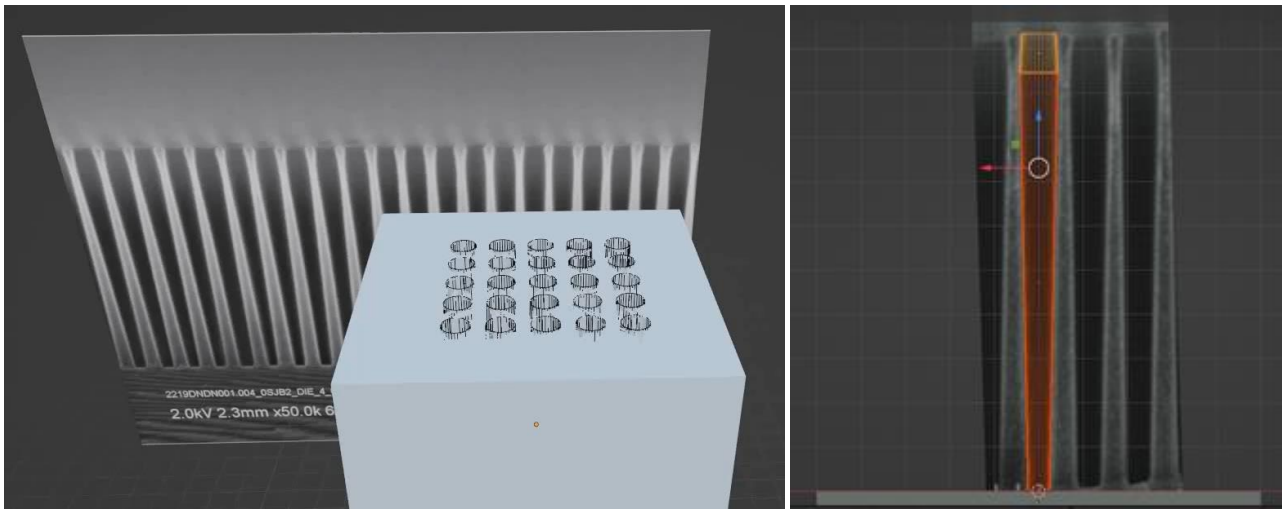


Figure 5: View of XSEM image of AMAG7 HAR hole 1 μm depth sample in SimuSEM GUI, to align the 2-cone profile model applicable to bowing profiled holes.

From the process above, the 1 μm depth structure by XSEM is expected to be 79 nm top CD, 88 nm mid CD 130 nm below top, depth 1030 nm, and bottom CD 48 nm but hole to hole variability at bottom can get as small as 40 nm bottom CD in some cases as the XSEM is not certain to be on same hole so representative statistics must be taken. Also the hole tilt is estimated as 0.1°. Likewise the 1.5 μm depth holes are also measured as top CD 82 nm, mid CD 88 nm at 130 nm below top, depth 1500 nm, and bottom CD 48 nm but as small as 35 nm, with tilt of 0.2°. HAR hole simulations were run to N=10000 certainty and 10 keV and matched against the experimental waveforms extracted from the images, and with a couple iterations of reducing the bottom CD, excellent matches between the simulated and experimental waveforms were found in all cases as shown in Figure 6, which achieved convergence when the hole we simulated for 1 μm depth was 40 nm in diameter at bottom, the 1.5 μm HAR hole was 35 nm at bottom, and also the tilts matched. The fits are a good match, including the asymmetry expected with tilted holes. Thus for 10 keV HAR hole case we achieve validation of the model.

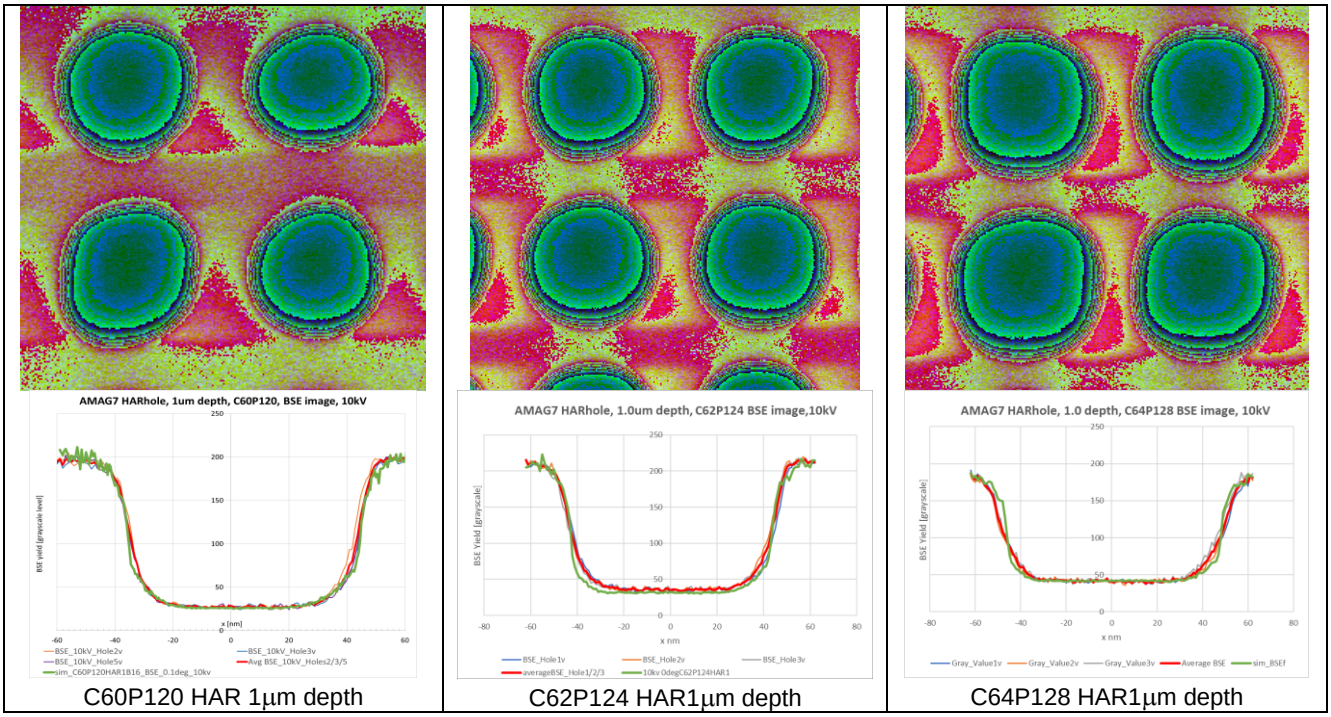


C60P120 HAR 1μm depth | C62P124 HAR1μm depth | C64P128 HAR1μm depth

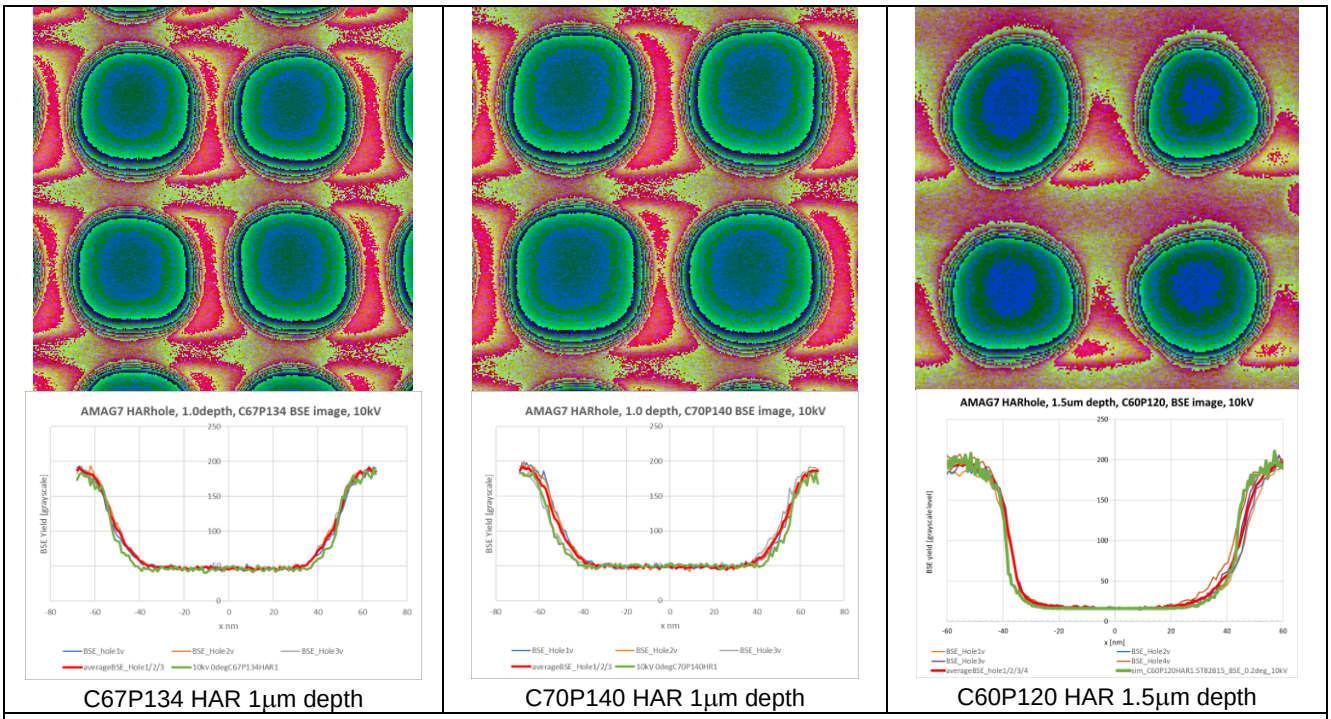


Figure 6: Magnified views of the NGR5000 HV-SEM images of the 6 AMAG7 HARhole features included in study, with stretched color scales to highlight the details of the very dim signal from the hole bottoms which give rich visualization of the hole's verticality, along with the graph of the grayscale linescan of BSE intensity across an average of the most typical holes and the simulated linescan by SimuSEM of the same hole, as achieved after a few iterations to match XSEM and topdown reference data.

A recent work in the literature [22-23] also explored HV-SEM imaging of HAR holes, including deeper holes down to 5 µm depth and at higher beam energies up to 45 keV. This work also left a good record of the exact cases and geometries and results, and thus is another good data set for validation studies in that regime. We replicate the cases shown in Figure 7, reprinted below. The main finding of [22-23] is that the BSE signal normalized to the hole top follows the trend of an exponential decay with depth down the hole for a given hole aspect ratio and sidewall angle, and in this work we strive to replicate that result as validation.

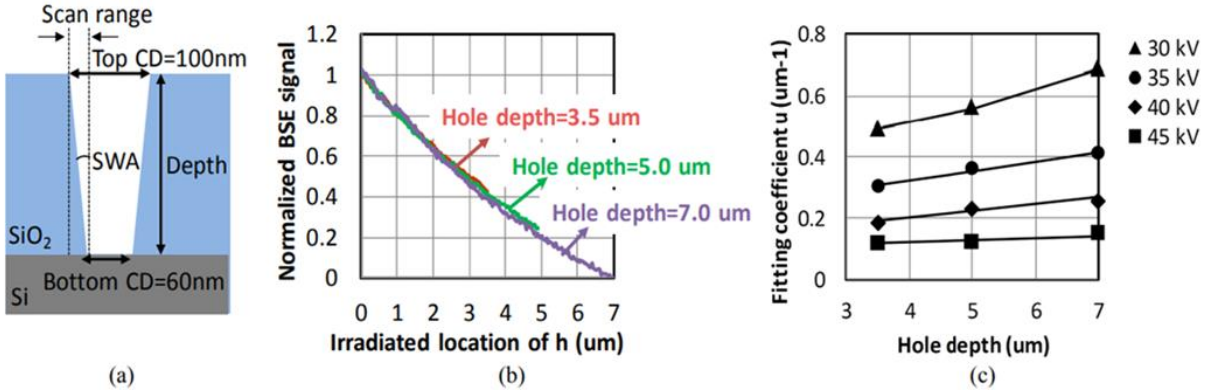


Figure 7 (reprinted from Figure 4 of [22]) (a) Cross-sectional view of the simulation models of the HAR holes (b) Examples of the normalized signal intensity as a function of the irradiation depth location in a hole with different depths at electron energy 45 keV. The hole density is 35% and the SWA is 0.16° for all. (c) Comparison of the dependence of the fitted coefficient µ on the depth of the hole, for the electron energy ranging from 30 to 45 keV.

The paper [22] defined the hole to simulate as 5000 nm $SiO_2$ film on Si substrate, with a top diameter of 100 nm, bottom diameter of 60 nm, and height all 5000 nm thru the $SiO_2$. We simulate this hole in SimuSEM by setting it up as a Boolean truncated cone Boolean subtracted from the $SiO_2$ film as shown in Figure 8, with 1 nm square pixels, N=10000

electrons per pixel, and 30 keV, 35 keV, 40 keV and 45 keV beams to get the BSE images shown in Figure 8. N=1000 would have been sufficient, however we wanted lots of statistics for the fits so erred on side of higher N.

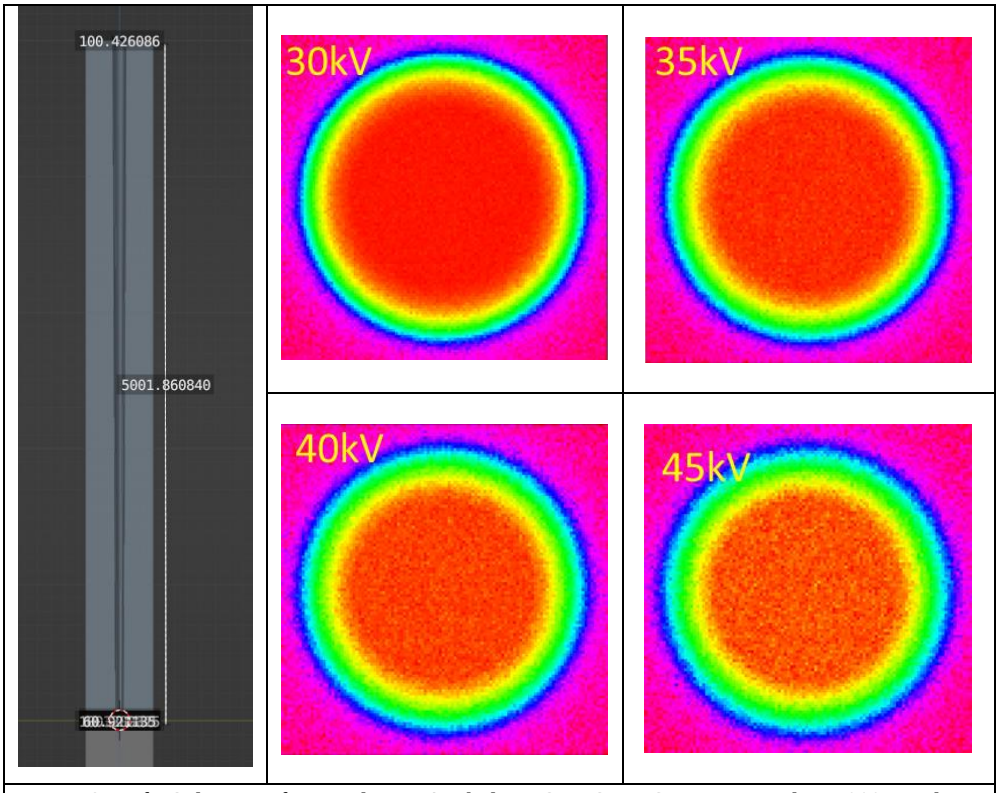


Figure 8: Left: Sideview of 5 μm deep HAR hole in SimuSEM GUI, measured as 5000 nm deep, 100 nm top CD and 60 nm bottom CD. Right: Colorized (spectrum scale) simulated images of 5 mm HAR hole for 30-45 keV beam energies.

With simulation, the exact height at each pixel is known by the user and is calculable. We thus can plot the BSE signal as a function of depth down the hole, and also for the previous AMAG7 HAR hole results at 10 keV and also simulated at 15 keV, as shown in Figure 9, where the exponential decay law of BSE signal from the hole depths is verified conclusively in all cases at all of the beam energies and different hole depths.

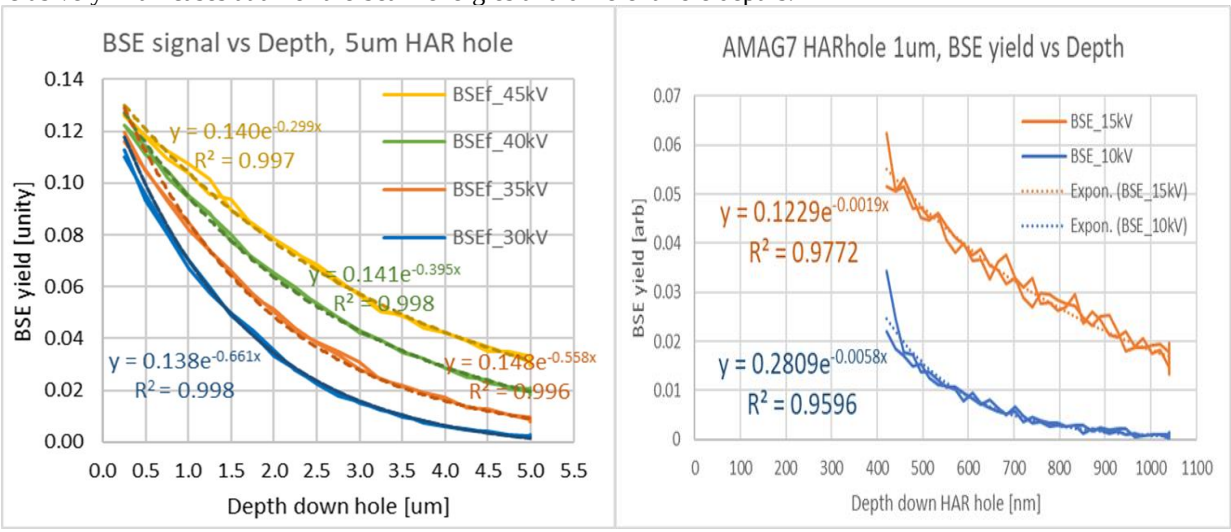


Figure 9: BSE yield correlated to depth down HAR holes from these simulations follow the observed exponential decay trend.

The paper [22] also gave specific results for the normalized BSE signal (with respect to hole top) as function of depth for 45 keV beam down their 5 μm hole, and overlaying our results also matches very conclusively to their results, which were validated both experimentally and by simulation by the original authors, and duplicated conclusively here. See the blue data points in Figure 10 below, which are the results from these simulations overlaid on top of the original results in the paper.

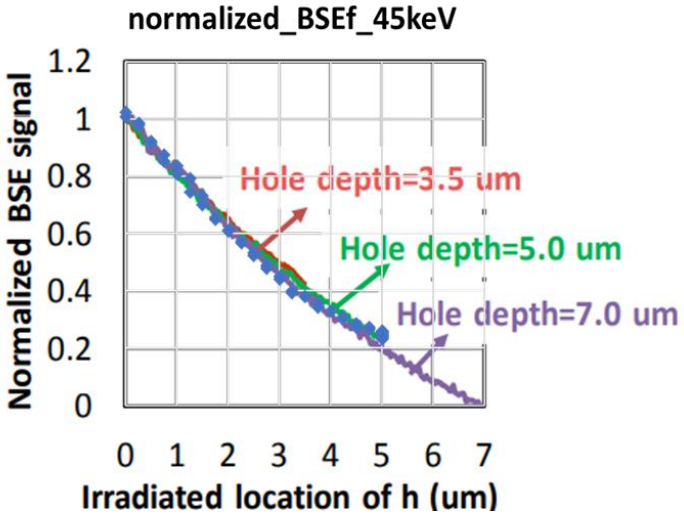


Figure 10: Simulation results from SimuSEM in blue conclusively match the previous results from [22], showing mutual validation.

The same paper [22] also demonstrated tilt imaging of bowing HAR holes 3.5 μm deep, and we also duplicate their results of tilt imaging at 30 keV beam at topdown and ±1° beam tilt. The hole they used had top CD of 276 nm, mid CD of 300 nm at depth of 1.3 μm, bottom CD of 140 nm, and depth of 3.5 μm.

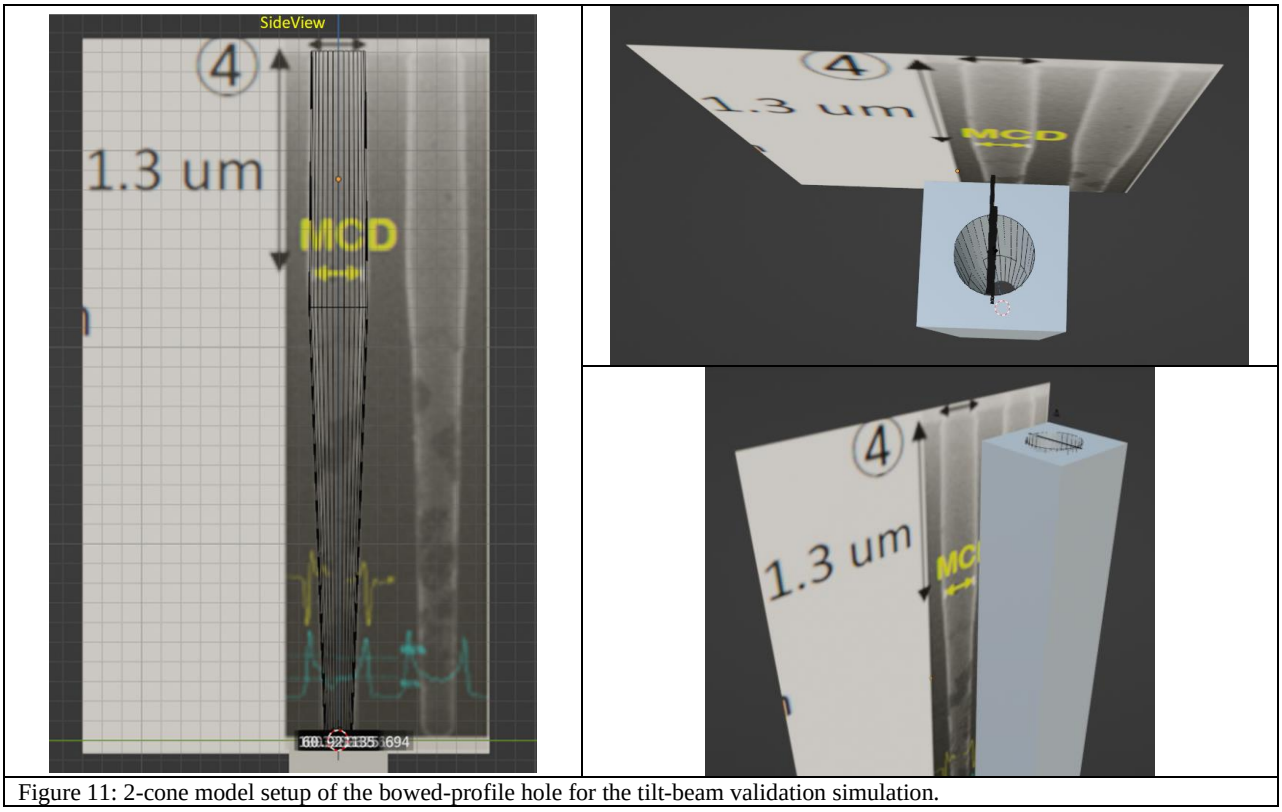


Figure 11: 2-cone model setup of the bowed-profile hole for the tilt-beam validation simulation.

The results of the tilt hole simulations are shown in Figure 12, and the images, while rotated on different axes, are good matches considering the grayscales (colorized for this paper) are not matched. The resulting linescans match well between the cases, which is another conclusive validation result.

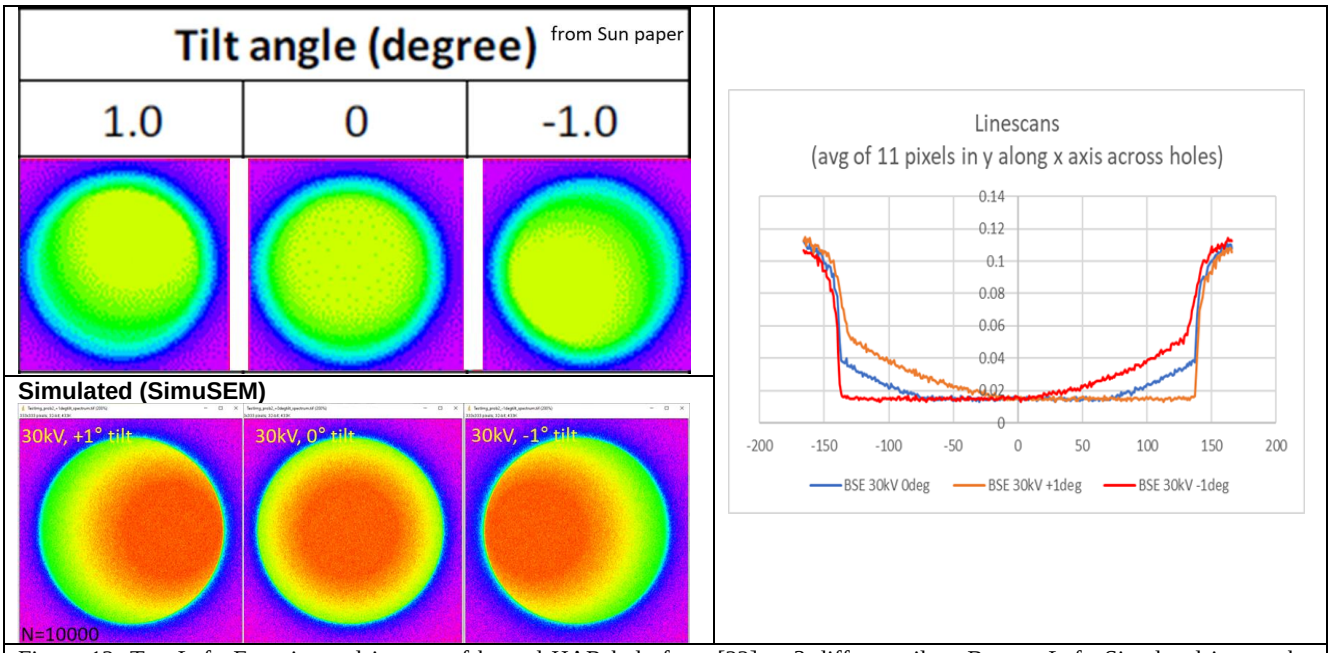


Figure 12: Top Left: Experimental images of bowed HAR hole from [22] at 3 different tilts. Bottom Left: Simulated images by SimuSEM of same exact cases, same image other than rotation and different brightness scale. Right: Linescans of the tilted holes from the simulations, behaving as expected.

With these conclusive validations of the HV-SEM simulation capabilities on HAR holes, we now can look at other HV-SEM problems with confidence of accuracy.

## SEE-THRU IMAGING OF METAL LINE GRATINGS

Another contemporary key topic which involves use of HV-SEM is calibrating optical overlay when aligning thru thick overlayer films, especially for stacks such as metal damascene. This topic has been modestly explored in past [14] but such studies are now much more feasible and practical than in past with the DOE and speed features of SimuSEM. The question that needs an answer is "what beam energy can accurately detect the center location of a buried feature or grating under *x* nm of oxide film". There are many different sample setups one could simulate for this problem set, so here we take 5 damascene metal lines of 30 nm width and 30 nm depth with 60 nm pitch, and on top of those is a

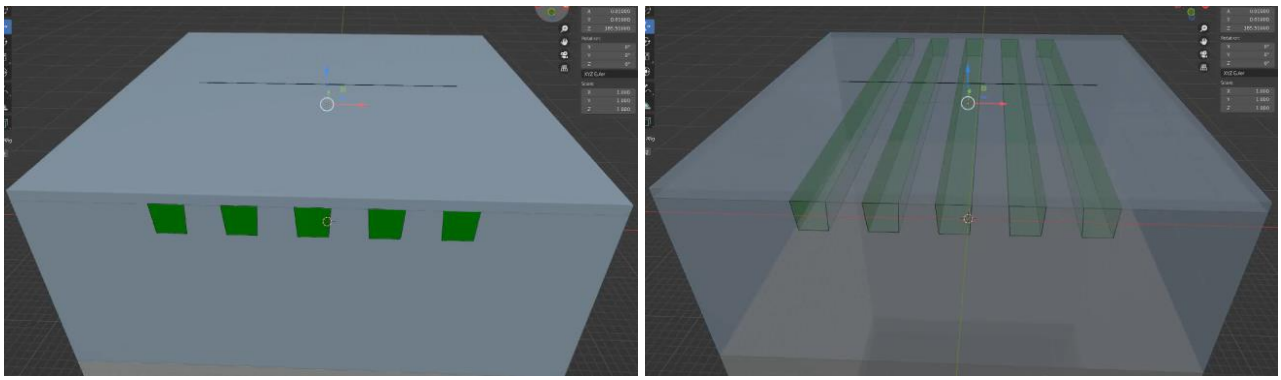

Figure 13: Left: Buried grating of 5 Cu lines embedded in $SiO_2$, with 30 nm CD, 60 nm pitch and 30 nm depth. The lines are trapezoidal fills of oxide with 2° sidewall angle as shown. The overlayer is an oxide film which is defined to be looped within the

simulation to different thicknesses so an entire DOE of buried grating depths can be run very simply. The thin line in the middle of the top face of the sample is the scan region of pixels which will be simulated as a linescan. Right: Transparent view of same structure.
variable-thickness $SiO_2$ film which can be looped to different defined thicknesses to efficiently allow a DOE study of the detectability of the metal lines and gratings; see Figure 13. Both copper (Cu) and tungsten (W) gratings were simulated. In these simulations the thickness of the variable film is 10 nm to 300 nm, with step 10 nm for each iteration, with 1 nm pixels, beam energies of 10 keV, 15 keV, 20 keV, 25 keV and 30 keV with N=10000 electrons per pixel to improve SNR as BSE signals are noisy due to their stochastic nature and not being so confined to the surface as with SE images, thus higher N needed to fully understand the baseline performance with BSE imaging. In the real world, measurements will be lower N but multiple linescans can be averaged over the grating to achieve similar SNR for linescans, and also more advanced filtering techniques might also be employed to improve SNR. However the simulations will lead to the best conditions for real world tools to attempt first and finetune from there.

Figure 14 shows simulated images at N=100 to show how the images appear from those linescans with 10 keV incident electron beam. The individual lines of the grating are clearly visible out to 110 nm of oxide overlayer, and the centroid is visible against the background to what appears visually to be somewhere slightly below 160 nm. Quantitatively, in Figure 15 below on the left side, the simulated linescans are shown for many values of the thickness of the oxide overlayer thickness, and the peaks, valleys and baseline background signal from outside the grating region is used to calculate the contrast of the grating vs the valleys or vs the background. The contrast of peak vs the background is the best metric for the contrast of the grating as it includes the "centroid" signal around the grating as part of what gives contrast to the background, and this is calculated as the peak BSE signal averaged over the 5 peaks above the lines, minus the background BSE level. Also the contrast of the peaks vs the valleys can be taken to explore how deep the lines are

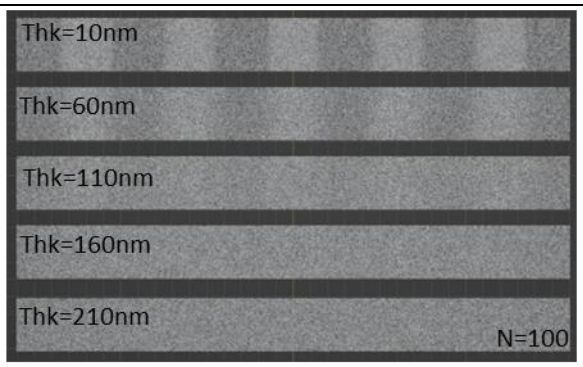


Figure 14: Simulated images of the copper grating through different $SiO_2$ film thicknesses.

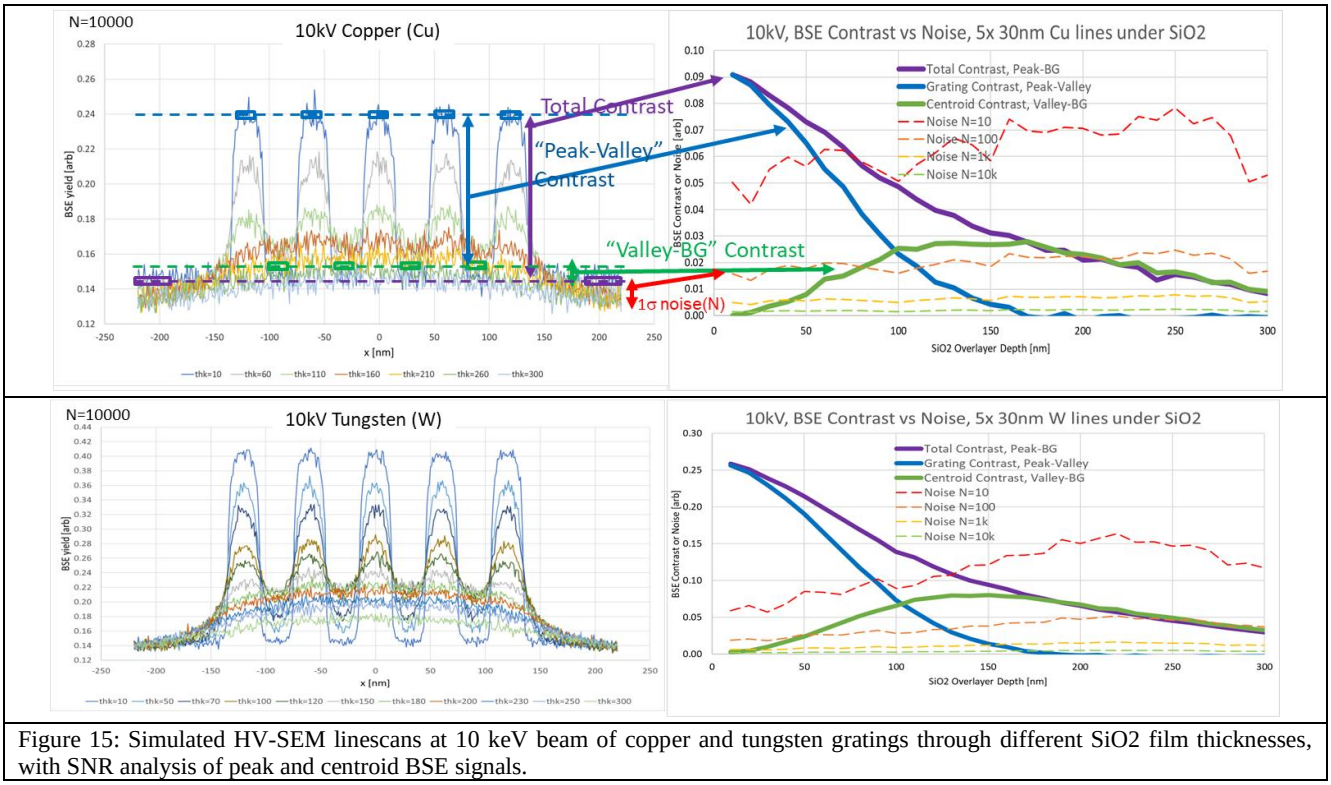


Figure 15: Simulated HV-SEM linescans at 10 keV beam of copper and tungsten gratings through different SiO2 film thicknesses, with SNR analysis of peak and centroid BSE signals.

resolvable. These contrast values are then normalized to the 1σ noise for the setting used (dependent on N value as square root of N) which allows us to calculate the SNR curve for all the depths of the oxide overlayer for each beam condition, for a full SNR analysis as shown in Figure 15 on the right side, for both copper and tungsten buried gratings.

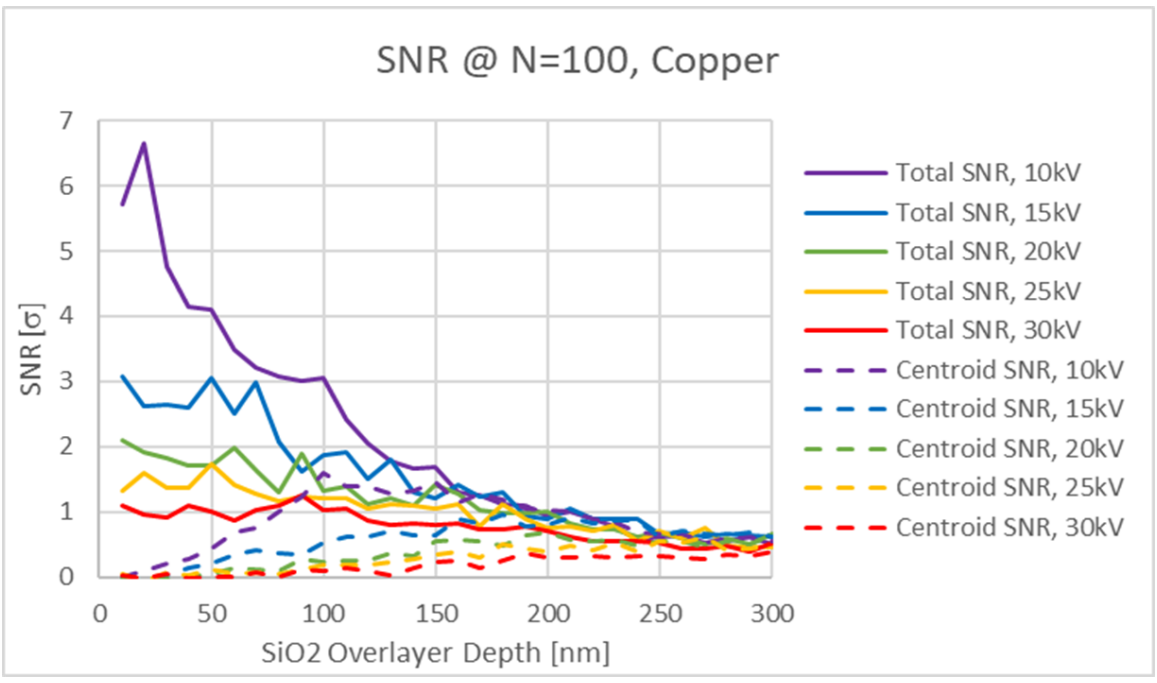


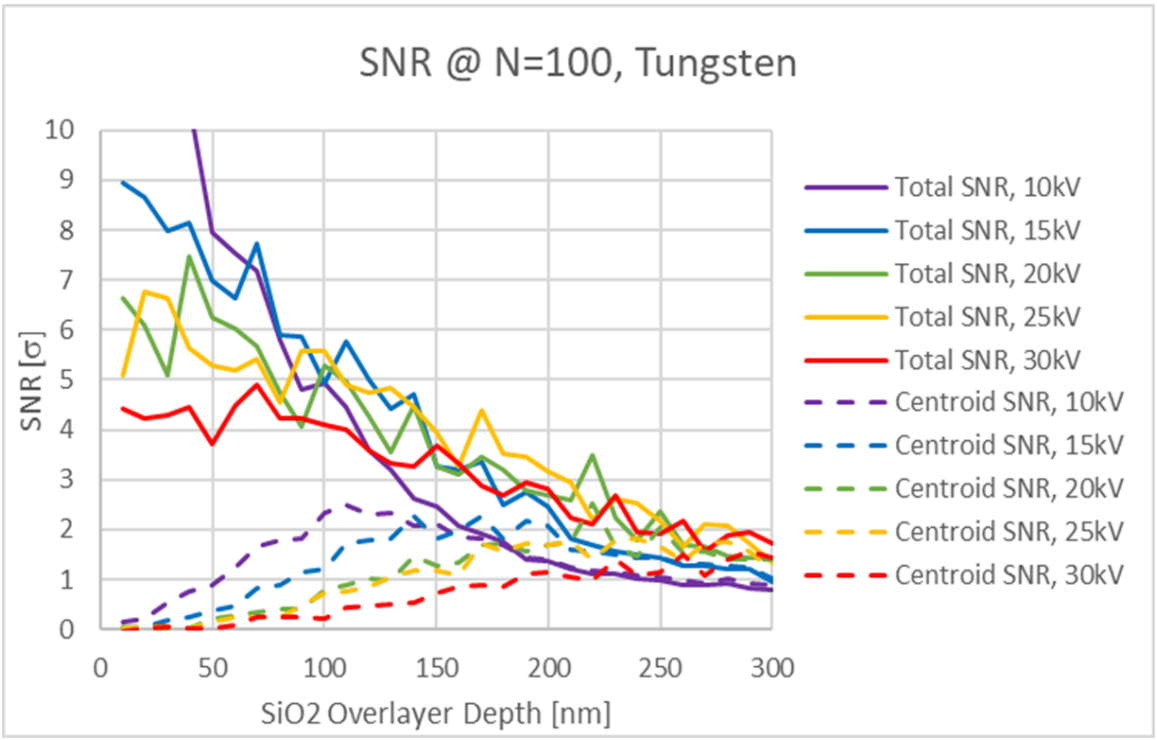


Figure 16: SNR analysis results for all beam energies simulated for the copper and tungsten buried gratings.

The above results predict, as contrast is larger than 1σ noise at N=100, that the copper grating will be visible at 10 keV beam down to ~180 nm thru the oxide, and tungsten grating down to ~220 nm thru oxide. This same analysis was

repeated for the other beam energies up to 30 keV, with noise at N=100 used to estimate the SNR vs depth for all of the beams, as shown in Figure 16. SNR should be 2 or 3 for good detectability, although with advanced filtering techniques on real tools this might be somewhat extendible. These results show copper visible with 10 keV beam being best, down to ~120 nm for good SNR, and for tungsten, the centroid is visible at 30 keV down to ~240 nm depth thru oxide.

## ONO INTENTIONAL DEFECT ARRAY BY HV-EBI

Past studies of EBI-SEM using JMONSEL are available in the literature.[11-12,14-19] Defectivity is a large yield detractor and is only getting harder to detect with complex 3D structures. HV-SEM see-thru techniques can detect buried voids, buried particles, surface damage or particles in trenches or holes. To explore examples of using HV-SEM in such a role and demonstrate how much more detailed intentional defect array (IDA) studies can get, a large test cell was designed within 2-3 hours in SimuSEM. The IDA (intentional defect array) consists of a 32 cycle ONO stack (10 nm thick individual layers of silicon oxide and nitride, alternating thru 32 cycles), with a big trench with multiple ledges and a hex array of contact holes, and defects were manually added in the forms of surface nodules, craters, pits and scratches and intrusions on different trench ledges and sidewalls down the trench, and also on surface between the holes. Also, particles are added, including a tungsten pyramid in the bottom of one of the contact holes, a 15 nm void 100 nm under the surface in the ONO stack, a 10 nm copper sphere 100 nm under the surface of the ONO stack, and a nitride sphere of 15 nm diameter 100 nm under the surface of the ONO stack, and also some of the contact holes are made tilted, small or one was not completely etched so bottom is nitride and not Si. As with the grating see-thru experiments simulations of images at different beam energies, a similar SNR study can be performed on each defect type to estimate what should be visible at different beam conditions and doses.

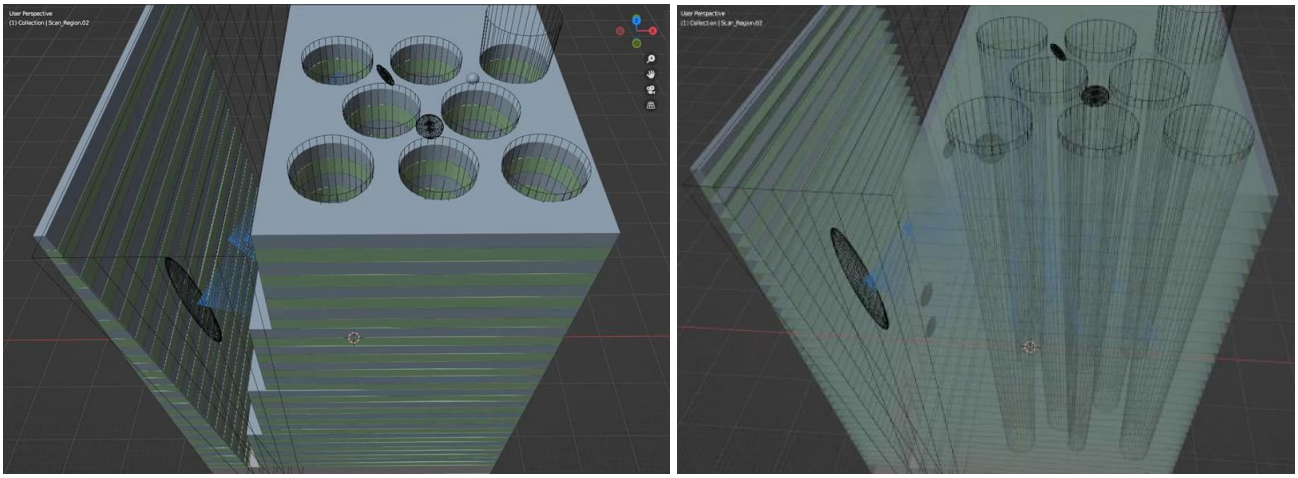

Figure 17a: Image gallery of ONO IDA.

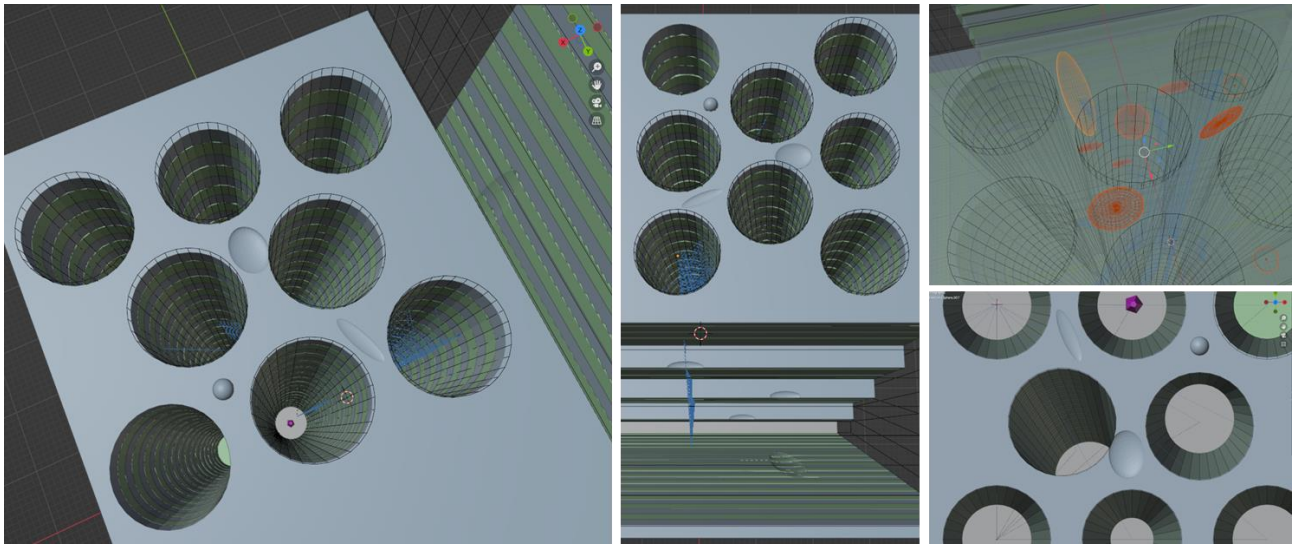

Figure 17b: Image gallery of ONO IDA.

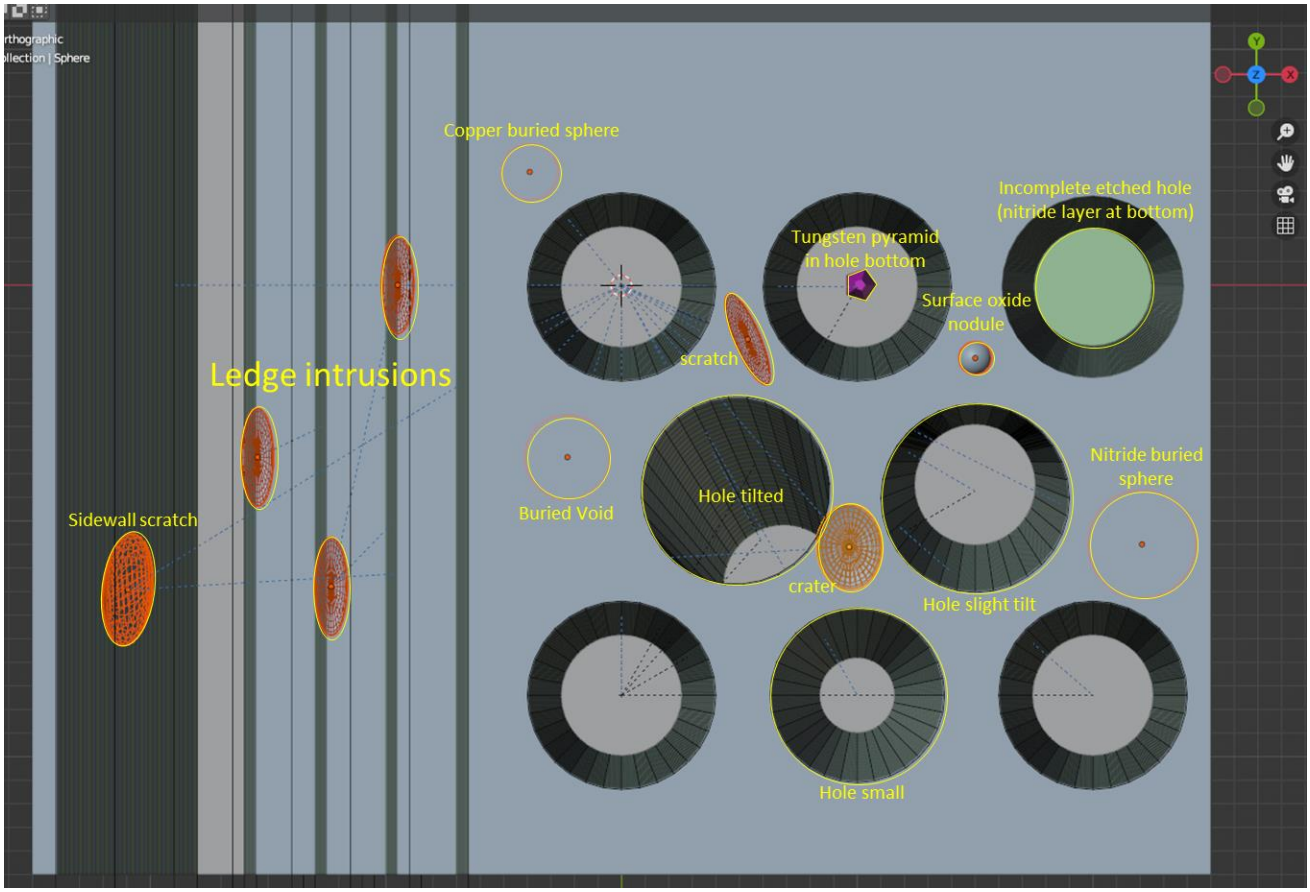


Figure 18: ONO IDA top plan view showing exact locations of all intentional defects.

The family of SE and BSE images from over the ONO IDA for N=100 electrons per pixel and beams of 500 V, 800 V, 2 keV, 5 keV, 10 keV, 15 keV and 20 keV are shown in Figure 19. Overlays of the locations of the intentional defects are also shown.

| SE images | BSE images |
| --- | --- |
| 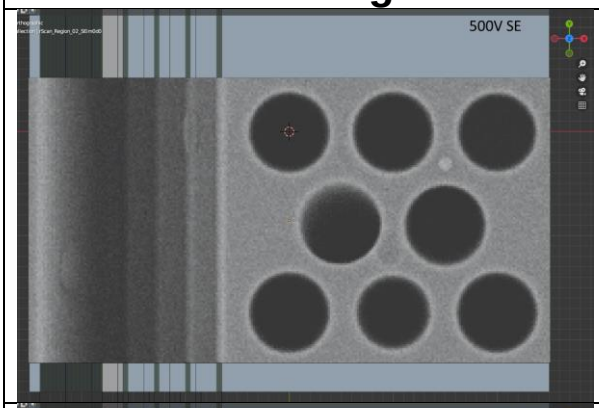 | 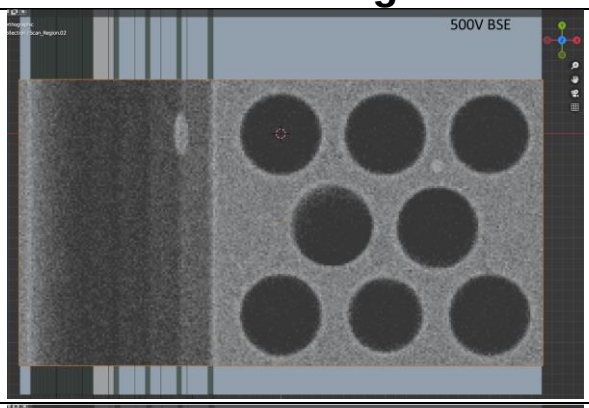 |
| 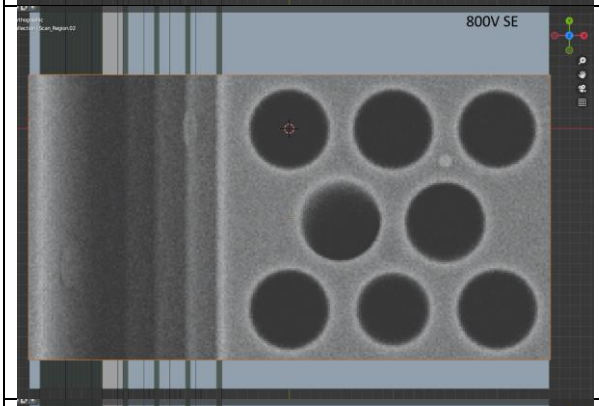 | 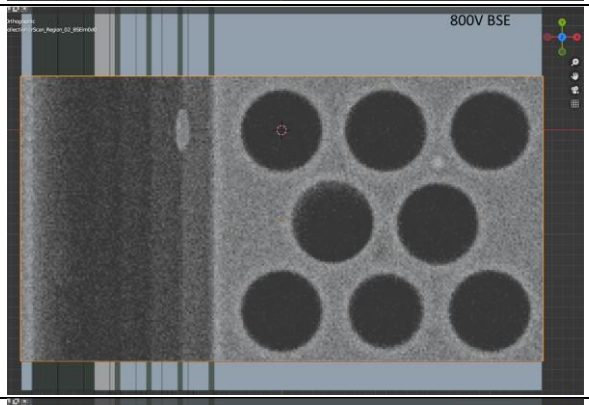 |
| 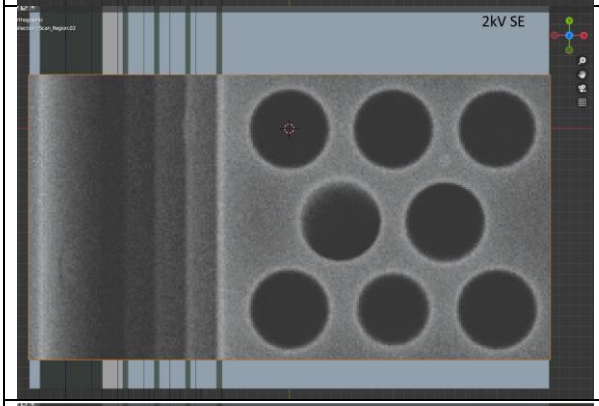 | 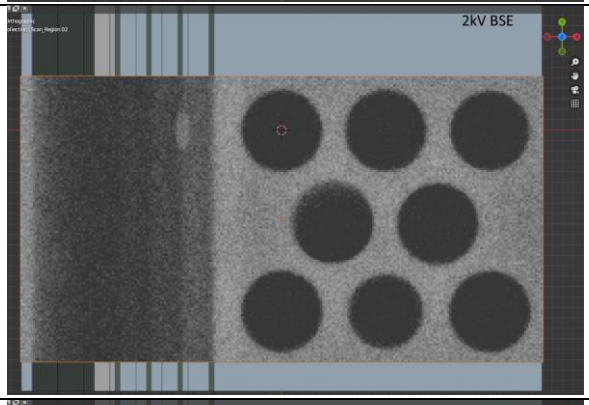 |
| 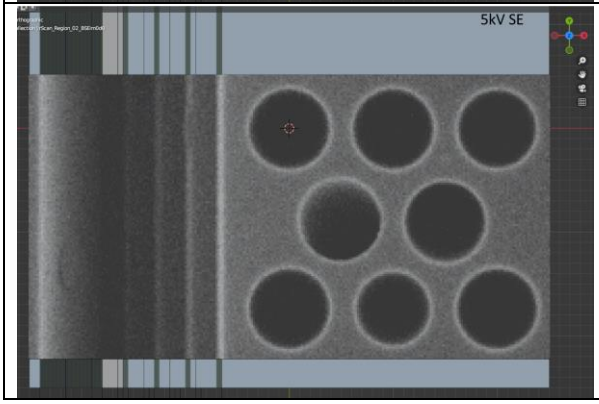 | 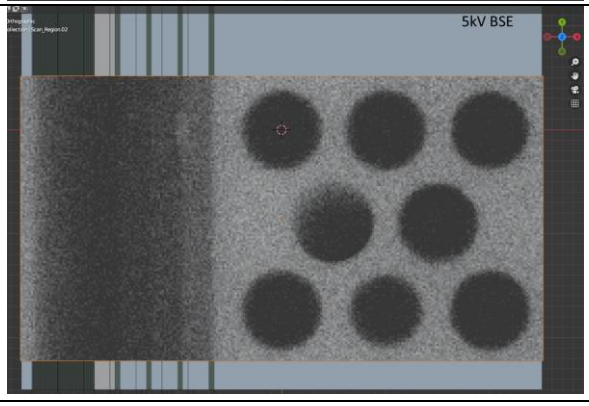 |

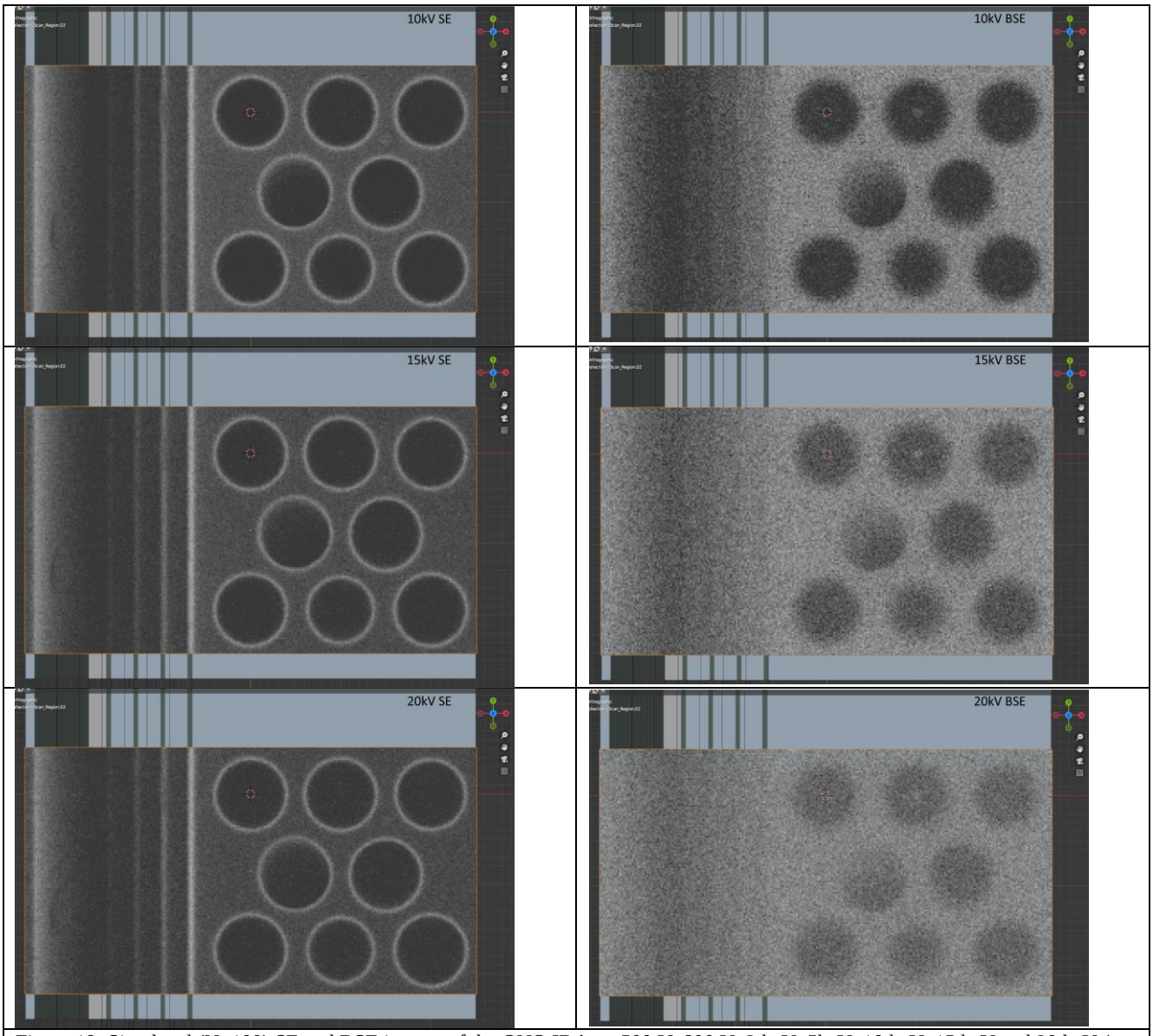


Figure 19: Simulated (N=100) SE and BSE images of the ONO IDA, at 500 V, 800 V, 2 keV, 5keV, 10 keV, 15 keV and 20 keV (top to bottom, respectively).

We explore these results quantitatively thru a similar SNR approach as used in the see-thru buried grating experiment, using references that are chosen to be typical background for analogic situations as on a ledge down the trench, of typical non-errant contact holes, and of surfaces between the holes for comparison to defective locations. The results of such an analysis are shown below for each defect type included in the ONO IDA in Figure 20, and summarized as to best SNR for each defect in Figure 21. As can be seen, most defect types had at least one condition where SNR > 1 (ideally > 3) so in theory those defects should be detectible, as filtering techniques and higher dose (higher N) can also be used to improve SNR. Further exploration of full DOEs of different defect types with different parameters such as depth can be performed, and such exhaustive studies, only practical using simulation, will be crucial to achieving capabilities to understand the capabilities, limits and best parameters for such work.

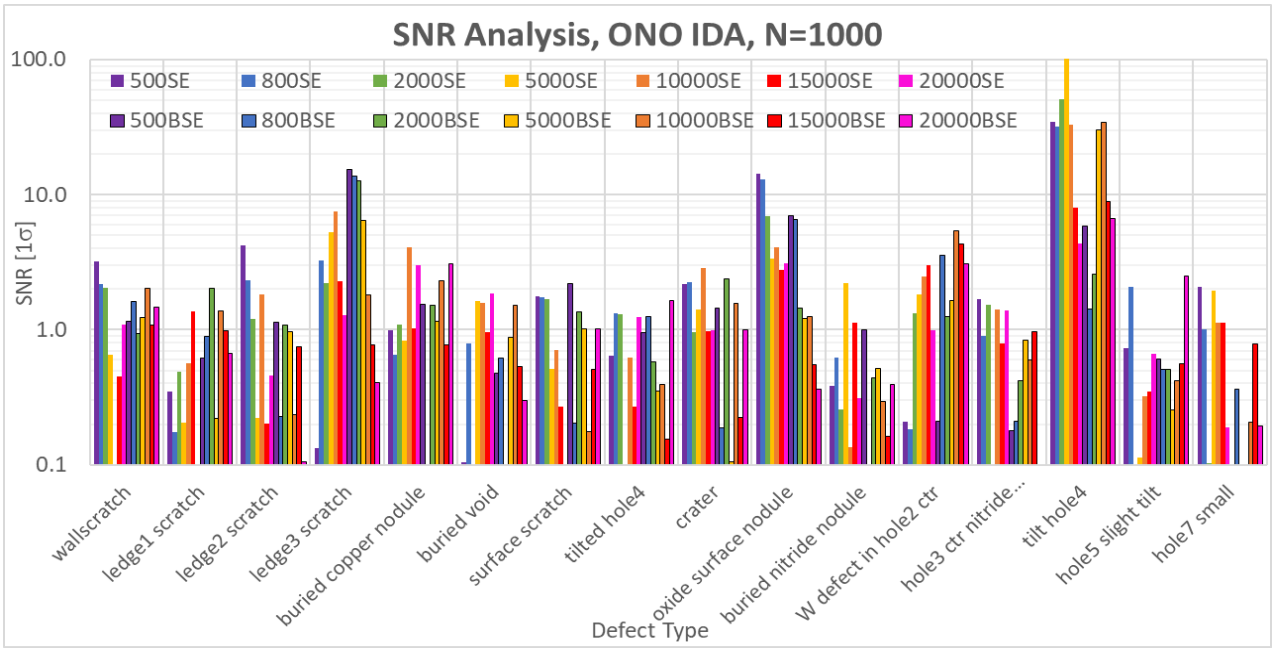


Figure 20: SNR for N=1000 for each defect type at each beam condition for both SE and BSE images, showing that a solution where SNR>2 is available for most of them.

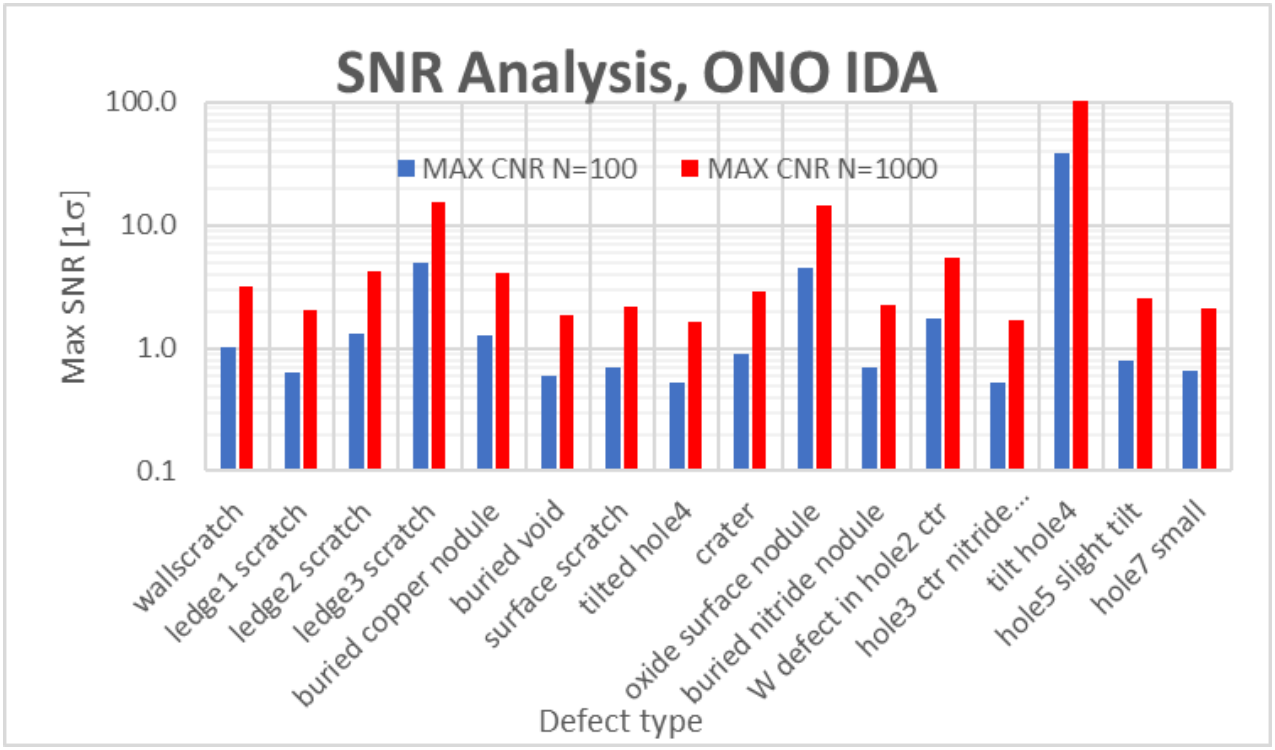


Figure 21: Best SNR observed for each defect type for N=100 or N=1000 doses.

## CONCLUSIONS

Multiple HV-SEM use cases were explored by simulation to demonstrate the widespread upcoming HV-SEM applications of importance that require in-depth quantitative studies to understand best tool parameters, methods and

capabilities for HAR hole imaging, see-thru imaging of buried features, and detectability of buried defects or defects in deep structures. Controlled experiments of these cases will be difficult and expensive, and simulation provides a very inexpensive and faster way to explore such parameterized problems thoroughly, with less uncertainty as "the answer is always known" inherently in simulation, allowing conclusions to be made from responses to intentional parameter variations.

HAR hole samples were physically imaged and simulated, and successful match between experimental and theoretical treatments was achieved for the whole gamut of HAR hole sizes from 1μm down to 5μm depths, including the previously-observed exponential decay trend of the BSE signals from different hole depths, and also successful tilt imaging was demonstrated and validated to another source. HV-SEM was also explored for see-thru imaging of buried copper and tungsten gratings, with a fast and efficient method demonstrated to quantify, thru SNR analysis, grating detectability as a function of buried depth, which will be an important capability for doing serious HV-SEM calibration efforts to support optical overlay on many advanced stacks. In this study, we determined that copper gratings should be visible at 10 keV beam down to 120 nm depth under oxide, and tungsten gratings down to 240 nm under oxide with good detectability of SNR>2.

Feasibility of defect detection of buried voids, particles and surface defects down holes/trenches in a complex 3D ONO IDA were also shown, with the capability to simulate full SNR DOEs within such complexity. Of the defects attempted in this 32 cycle ONO stack, most had at least one beam energy where the defect could be detected with SNR>2 or close, with ability to increase N for better detectability. Future work will include a detailed DOE of detectability of such defects at different depths.

## ACKNOWLEDGEMENTS

AMAG Consulting, LLC (dba AMAG nanometro) thanks Dr. John S. Villarrubia of the National Institute of Standards and Technology (NIST) in Gaithersburg, Maryland, USA. Dr. Villarrubia is the creator of the JMONSEL SEM simulation software that is the physics core and basis for SimuSEM. Also we thank Andras Vladár of NIST for many HV-SEM discussions. We also acknowledge Mark Raymond, Patrick Kearney, Harlan Stamper, Brian Martinick, Ilyssa Wells, Dominic Ashworth and Frank Tolic of NYCreates for AMAG7 HARhole wafer process development and production, and also Dr. David Klotzkin of SUNY Binghamton for various guidance.

## REFERENCES

[1] Liddle, J. A., Hoskins, B. D., Vladár, A. E. and Villarrubia, J. S. "Research Update: Electron beam-based metrology after CMOS", APL Materials 6, 070701 (2018); https://doi.org/10.1063/1.5038249 .
[2] J.S. Villarrubia, et al., "Scanning electron microscope measurement of width and shape of 10 nm patterned lines using a JMONSEL-modeled library", Ultramicroscopy (2015), http://dx.doi.org/10.1016/j.ultramic.2015.01.004 .
[3] Brad Thiel, Michael Lercel, Benjamin Bunday, and Matt Malloy, "Assessing the Viability of Multi-Electron Beam Wafer Inspection for sub-20 nm Defects", Proc. SPIE 9236, Scanning Microscopies 2014, 92360E (2014); doi:10.1117/12.2069302.
[4] Villarrubia, J. S. , Ritchie, N. W. M., and Lowney, J. R. "Monte Carlo modeling of secondary electron imaging in three dimensions," *Proc. SPIE* **6518**, 65180K (2007).
[5] J. R. Lowney, A. E. Vladár, and M. T. Postek, "High-accuracy critical-dimension metrology using a scanning electron microscope," Proc. SPIE 2725, pp. 515-526 (1996); J. R. Lowney, "Application of Monte Carlo simulations to critical dimension metrology in a scanning electron microscope," Scanning Microscopy 10, pp. 667-678 (1996).
[6] J. S. Villarrubia and Z. J. Ding, "Sensitivity of SEM width measurements to model assumptions," Proc. SPIE 7272 (2009).
[7] Villarrubia, J. S., and Ding, Z. J. "Sensitivity of SEM width measurements to model assumptions," *J. Micro/Nanolith. MEMS MOEMS* **8**, 033003 (2009).
[8] Aron Cepler, Benjamin Bunday, Bradley Thiel, John Villarrubia. "Scanning electron microscopy imaging of ultra-high aspect ratio hole features". Metrology, Inspection, and Process Control for Microlithography XXVI. Proceedings of the SPIE, Volume 8324, pp. 83241N-83241N-14 (2012).

[9] J.S. Villarrubia, A.E.Vladár, B.Ming, R.J.Kline, D.F.Sunday, J.S.Chawla, and S.List, "Scanning electron microscope measurement of width and shape of 10 nm patterned lines using a JMONSEL-modeled library," Ultramicroscopy 154 (2015) 15. http://dx.doi.org/10.1016/j.ultramic.2015.01.004
[10] Bunday, Benjamin D. "Noise fidelity in SEM simulation". Proc. SPIE, Volume 11325, Metrology, Inspection, and Process Control for Microlithography XXXIV; 113250R (2020). https://doi.org/10.1117/12.2559631
[11] Bunday, B., Mukhtar, M., Quoi, K., Thiel, B., and Malloy, M. "Simulating Massively Parallel Electron Beam Inspection for sub-20 nm Defects". Proceedings of SPIE Vol. 9424, 94240J (2015).
[12] Bunday, Benjamin D., Klotzkin, S., Patriarche, D., Mukhtar, M., Maruyama, K., Kang, SK, Yamazaki, Y. "Simulating process subtleties in SEM imaging". Proceedings Volume 12053, Metrology, Inspection, and Process Control XXXVI; 120530A (2022) https://doi.org/10.1117/12.2615753 .
[13] Bunday, Benjamin D. "Metrology test artifact availability improvement", Proceedings Volume 12053, Metrology, Inspection, and Process Control XXXVI; 120531C (2022) https://doi.org/10.1117/12.2615726 .
[14] Benjamin Bunday, Abner Bello, Eric Solecky & Alok Vaid, "7/5 nm logic manufacturing capabilities and requirements of metrology", Proc. SPIE 10585, Metrology, Inspection, and Process Control for Microlithography XXXII, 105850I (22 March 2018); doi: 10.1117/12.2296679
[15] Maseeh Mukhtar, Benjamin Bunday, Kathy Quoi, Matt Malloy & Brad Thiel. "Measuring multielectron beam imaging fidelity with a signal-to-noise ratio analysis", J. Micro/Nanolith. MEMS MOEMS 15(3) 034004 doi: 10.1117/1.JMM.15.3.034004, Published in: Journal of Micro/Nanolithography, MEMS, and MOEMS Volume 15, Issue 3 (23 August 2016).
[16] Aron Cepler, Benjamin Bunday, Bradley Thiel &John Villarrubia. "Scanning electron microscopy imaging of ultra-high aspect ratio hole features". Metrology, Inspection, and Process Control for Microlithography XXVI. Proceedings of the SPIE, Volume 8324, pp. 83241N-83241N-14 (2012).
[17] Maseeh Mukhtar, Bradley Thiel & Benjamin Bunday. "Backscattered electron simulations to evaluate sensitivity against electron dosage of buried semiconductor features", Proc. SPIE. 10585, Metrology, Inspection, and Process Control for Microlithography XXXII (2018).
[18] Thiel, B., Mukhtar, M., Quoi, K., Bunday, B., & Malloy, M. (2016). "Patterned Wafer Inspection with Multi-beam SEM Technology", Microscopy and Microanalysis, 22(S3), 586-587. doi:10.1017/S1431927616003780
[19] Benjamin Bunday, Maseeh Mukhtar, Kathryn Quoi, Bradley Thiel, & Matt Malloy. "Simulating Massively Parallel Electron Beam Inspection for sub-20 nm Defects". Proceedings of SPIE Vol. 9424, 94240J (2015).
[20] See details on Blender at website: https://www.blender.org/.
[21] J. S. Villarrubia, "Model validation for scanning electron microscopy", Proc. SPIE 12496-26 (2023, publishing pending).
[22] Wei Sun, Yasunari Sohda, Hiroya Ohta, Taku Ninomiya, Yasunori Goto, "High voltage CD-SEM based metrology for 3D-profile measurement using depth correlated BSE signal," Proc. SPIE 10959, Metrology, Inspection, and Process Control for Microlithography XXXIII, 1095915 (26 March 2019); doi: 10.1117/12.2511272
[23] Wei Sun, Hiroya Ohta, Taku Ninomiya, Yasunori Goto, "High-voltage CD-SEM-based application to monitor 3D profile of high-aspect-ratio features," Journal of Micro/Nanolithography, MEMS, and MOEMS, Vol. 19, Issue 2, 024002 (May 2020). https://doi.org/10.1117/1.JMM.19.2.024002